JGR Oceans

RESEARCH ARTICLE
10.1029/2020JC016732

MJO Wind Energy and Prediction of El Niño

Nicholas D. Lybarger[1,2], Chul-Su Shin[1,3], and Cristiana Stan[1]

[1]Department of Atmospheric, Oceanic, and Earth Sciences, George Mason University, Fairfax, VA, USA, [2]Now at National Center for Atmospheric Research, Boulder, CO, USA, [3]Center for Ocean-Land-Atmosphere Studies, Fairfax, VA, USA

Key Points:
- MJO-ENSO relationship can be used to forecast El Niño events
- MJO-ENSO relationship can be used to diagnose model deficiencies in simulating the air sea interactions
- *MaKE* and *MaKI* indices are useful El Niño predictors

Correspondence to:
C. Stan,
cstan@gmu.edu

Citation:
Lybarger, N. D., Shin, C.-S., & Stan, C. (2020). MJO wind energy and prediction of El Niño. *Journal of Geophysical Research: Oceans*, *125*, e2020JC016732. https://doi.org/10.1029/2020JC016732

Received 21 AUG 2020
Accepted 22 SEP 2020
Accepted article online 28 SEP 2020

Abstract This study applies the energetic framework developed to quantify the interaction between the Madden-Julian Oscillation (MJO) and El Niño–Southern Oscillation (ENSO) to El Niño forecasting. The MJO wind power, measured by the covariability of MJO-related wind stress and oceanic Kelvin wave activity, is combined with the sea surface temperature (SST) anomalies, and two new indices are proposed. The MJO-Kelvin wave-ENSO (*MaKE*) index is proposed as an ENSO predictor and is shown to slightly outperform Niño 3.4 when applied to observational data sets and to greatly outperform Niño 3.4 when applied to CFSv2 reforecasts of the years 1980–2014. The MJO-Kelvin wave Influence (*MaKI*) index is proposed to predict MJO influence on developing El Niño events. This index performs reasonably well when applied to observations. The forecast skill of *MaKI* in the CFSv2 reforecasts suggests that this model does not predict the observed MJO-ENSO relationship as measured by this index.

1. Introduction

On time scales less than a decade, climate variability in the tropical Pacific is dominated by two phenomena: El Niño–Southern Oscillation (ENSO) on interannual (2- to 7-year) time scales and tropical oscillations on intraseasonal (30- to 90-day) time scales. ENSO variability occurs primarily in the central and eastern tropical Pacific, where sea surface temperatures (SSTs) in the cold tongue region are warmed (cooled) during El Niño (La Niña) due to a deepening (shoaling) of the eastern tropical Pacific thermocline (Wang et al., 2017). During the boreal winter, the Madden-Julian Oscillation (MJO) is the predominant tropical intraseasonal oscillation (Zhang, 2005). The MJO consists of an envelope of alternating enhanced and suppressed convective activity originating in the Indian Ocean and propagating eastward across the western Pacific. In the enhanced convective phase, winds at the surface converge and diverge at the top of the atmosphere. The wind pattern is reversed in the suppressed convective phase (Rui & Wang, 1990). The occurrence of the MJO is highly episodic (Waliser & Coauthors, 2009) and is typically categorized by its signal in precipitation anomalies, as well as by 200- and 850-mb zonal wind anomalies (Wheeler & Hendon, 2004; Zhang, 2005). MJO convective activity results in anomalous westerly surface winds in the western Pacific (Hendon et al., 2007) driven by two cyclonic systems located to the north and south of equatorial convection (Rui & Wang, 1990).

Efforts to identify a statistically significant linear relationship between MJO and ENSO have proven elusive (e.g., Hendon et al., 1999; Kessler, 2001; Slingo et al., 1999), though there is a seasonal dependence to this relationship (Hendon et al., 2007; McPhaden et al., 2006) that suggests a link between boreal spring/summer MJO activity and the peak of El Niño in boreal autumn/winter (Hendon et al., 2007; Tang & Yu, 2008). Although the MJO peaks primarily in boreal winter (December to March), there is a secondary peak in boreal summer (June to September) (Zhang & Dong, 2004), which could be more important for El Niño prediction given the fact that many operational forecast models suffer from the so-called "predictability barrier" in boreal spring (Jin et al., 2008). These earlier studies suggest that the lagged relationship between spring/summer MJO activity and autumn/winter ENSO variability is due primarily to two mechanisms: (i) downwelling oceanic Kelvin waves forced by MJO activity in the western/central tropical Pacific (Enfield, 1987; Hendon et al., 1998; Zhang, 2001) and (ii) a positive feedback between surface westerly wind anomalies associated with enhanced MJO activity in the western Pacific and warm SST anomalies in the central and eastern tropical Pacific (Hendon et al., 2007; Tang & Yu, 2008). In the second mechanism, westerly wind anomalies in the western tropical Pacific advect surface warm water from the warm pool into the tropical central/eastern Pacific, inducing a local change of SST gradient and reinforcing the westerly wind anomalies (Hendon et al., 2007; Tang & Yu, 2008). In the lead up to El Niño, wind stress variance that is uncoupled to SST

anomalies in the western tropical Pacific (i.e., the residual wind stress variability once the influence of SST anomalies has been removed via linear regression) is found to shift eastward toward the central Pacific. In this region, MJO explains more than two thirds of the thermocline variability while accounts for only half of the wind stress variance (Batstone & Hendon, 2005). This suggests that the MJO, as a spatially and temporally coherent wind stress signal, influences the ocean more strongly than less coherent wind stress forcing (Hendon et al., 2007; Kessler et al., 1995; Zhang & Gottschalck, 2002).

Nonetheless, the relationship between ENSO and subseasonal variability of the tropics is an open question. Some recent studies (Capodonti et al., 2018; Zhao et al., 2019) have questioned the effectiveness of subseasonal wind anomalies to force ENSO events, as the Kelvin wave field generated by subseasonal wind anomalies appears to be only a small fraction of the interannual Kelvin wave signal. Lybarger and Stan (2019, LS19 thereafter) argue that MJO associate wind power can affect the available potential energy of the ocean in certain conditions. LS19 suggest that the primary source of the MJO-Kelvin wave-ENSO relationship is the coincident phasing or resonance between westerly wind anomalies due to MJO activity and downwelling Kelvin waves during April-May-June (AMJ). The oceanic Kelvin waves can be due to direct excitation from MJO wind anomalies (McPhaden, 1999), excitation from wind anomalies unrelated to the MJO (Hu et al., 2014; Lian et al., 2014), or produced by internal ocean dynamics such as Rossby wave reflection off the western boundary of the tropical Pacific (Cravatte et al., 2004; Spall & Pedlosky, 2005).

The first objective of this study is to develop a method for holistically representing the MJO-ENSO relationship by creating indices that incorporate the covariability of MJO wind stress, Kelvin wave activity, and SST anomalies. The second objective is to demonstrate the applicability of these indices to seasonal forecast systems for El Niño prediction. Development of these indices draws upon the work of Lybarger and Stan (2018), which introduced a method for quantifying the influence of MJO-Kelvin wave covariability on the growth and peak of El Niño. Section 2 will describe the observational data sets and the operational forecasting data sets used in this study, as well as the statistical methods used to develop the new indices. Section 3 will discuss the results of applying these indices to observations and to an operational seasonal forecast model, followed by conclusions and discussion in section 4.

2. Data and Methods

2.1. Data Sets

Due to the need for long-term, daily observations in order to capture MJO variability during as many El Niño events as possible, two wind stress data sets are used here. The Blended Sea Winds wind stress product (Quick Scatterometer, QSCAT) from the National Centers for Environmental Information (NCEI) contains high-resolution (0.25° × 0.25°) daily scatterometer data from multiple satellite sources at daily time scales covering 9 July 1987 to 30 September 2011 (Peng et al., 2013; Zhang et al., 2006). Daily-averaged, high-resolution (0.25° × 0.25°) wind stress fields estimated from the Advanced Scatterometer (ASCAT, DASCAT) retrievals are obtained from the Centre de Recherche et d'Exploitation Satellitaire (CERSAT), at IFREMER, Plouzané (France) (Bentamy & Fillon, 2012). The latter covers the period from 21 March 2007 to the present, but for this analysis, only the period until 31 December 2016 is used. For the overlapping period of 21 March 2007 to 30 September 2011, the gridded linear average of the two data sets is used instead. Because QSCAT comes from multiple sources and is further supplemented by National Centers for Environmental Prediction (NCEP) Reanalysis 2 (Kanamitsu et al., 2002) to fill in missing data, there are no coverage problems related to sparse satellite swathes. However, DASCAT comes from a single source and therefore does suffer these problems. To counteract this, DASCAT is supplemented by QSCAT in the overlapping period and is interpolated in time to cover missing periods thereafter. There is rarely a period of more than a few days interpolated in this way. Furthermore, there are some unrealistically extreme wind stress data during certain conditions, which had to be eliminated. Values larger than ± 5 N m^{-2} have been replaced by this value. This threshold allows for the simple removal of exceedingly unrealistic values, while almost assuredly leaving realistic values untouched. Wind stress values exceeding 5 N m^{-2} would imply ocean current speed and boundary layer wind speed differ by ~70 m/s, which only occurs during the most extreme hurricanes. Considering the rarity of such events, and the long-term analyses performed here, this cutoff threshold is determined to be adequate for our purposes.

Ocean observations are also required for this analysis. Unfortunately, long-term, high temporal resolution ocean current and SST observations are difficult to obtain, so a reanalysis data set will be used as a proxy for observations. The Global Ocean Data Assimilation System (GODAS) (Nishida et al., 2011; Saha et al., 2006) covers the period 1979 to present, but only 1988–2016 will be used, due to the limitations imposed by the availability of the wind stress fields discussed above. GODAS has pentad temporal resolution and a spatial resolution of 1° × 1°. Analysis done over the overlapping periods show general agreement between surface wind stress fields from GODAS and the scatterometer data (not shown) and thus are determined to be reasonable approximation of observations, as found by Nishida et al., 2011, who validated GODAS fields and found them to be appropriate for oceanographic studies, excepting the salinity data that are not used for this analysis. GODAS is interpolated in time from pentad to daily resolution. DASCAT and QSCAT are interpolated in space to match the 1° × 1° resolution of GODAS. In the following discussions, this combination of DASCAT and QSCAT wind stress with GODAS SST and surface currents will be referred to by the catch-all term "observations."

The analyses done for observations are also performed for the NCEP Climate Forecast System, Version 2 (CFSv2) (Saha et al., 2014) reforecasts of each year during the period 1980–2014 (Huang et al., 2017, 2019). Each reforecast consists of five ensemble members initialized in early April and run for 3 months, from which daily wind stress, surface currents, and SST are retained. For further information on these reforecasts, see Huang et al. (2017, 2019).

2.2. MJO Wind Power

The MJO influence on ENSO is investigated in the ocean energetics framework pioneered by Goddard and Philander (2000) and applied by other studies to evaluate the effect of surface winds on ENSO dynamics in models and observations (e.g., Brown et al., 2011; Brown & Fedorov, 2010; Fedorov, 2002; Fedorov et al., 2003; Giese & Ray, 2011; Hu et al., 2014; Kim et al., 2011; Li et al., 2011; Lybarger & Stan, 2018; Masuda et al., 2015). In this framework, surface winds work against ocean pressure gradients to generate vertical motion of the mass field in the ocean and thus perturb the thermocline depth. The energy associated with the surface winds is measured by the wind power and perturbations in the thermocline depth are measured by the available potential energy. See Brown and Fedorov (2010) for a summary of the energy cycle of surface winds and ENSO.

To describe the variability associated with the MJO influence on oceanic Kelvin wave variability, the $W_{MJO,K}$ index (Lybarger & Stan, 2018, LS18 hereafter) is used. This index captures the wind power generated as the MJO wind stress supplies energy to (removes energy from) the ocean by acting in the same (opposite) direction as the surface currents. Here, the $W_{MJO,K}$ index is computed for observations in precisely the same way as LS18. First, the daily climatology (defined over the full time series from 1 January 1988 to 31 December 2016 for each grid point) of wind stress and surface currents is removed from each grid point to produce daily anomalies of these fields. Next, intraseasonal variability is separated from wind stress anomalies using the same method as Zhang and Gottschalck (2002). In this method, the daily wind stress anomalies are band-pass filtered to retain variability between 30 and 90 days. A Hilbert singular value decomposition (HSVD) analysis is then applied to these filtered data, isolating the primary modes of oscillatory signals. HSVD is regular singular value decomposition (SVD) analysis of a field and its Hilbert transform. The four HSVD leading modes are shown in Figure 2, and a brief physical interpretation is presented later. The first four principal components (PCs) of the HSVD decomposition are then projected onto the filtered wind stress and combined, giving $\tau_{MJO}(x, y, t)$ (Zhang & Gottschalck, 2002). Kelvin wave variability is then isolated from the ocean surface currents by projecting the meridional structure of a Kelvin wave (Kirtman, 1997) onto the daily zonal surface current anomalies, giving $u_K(x, y, t)$. The gridded product of these terms gives the MJO wind power generated through the interaction of these winds with the Kelvin waves in the surface currents. $W_{MJO,K}$ is then computed by taking the gridded product of MJO wind stress and ocean current anomalies associated with Kelvin wave activity ($\tau_{MJO}(x, y, t) \cdot u_K(x, y, t)$). The $W_{MJO,K}$ index is the area average of $W_{MJO,K}$ over the 1°S to 3°N and 175°E to 160°W domain, which is referred to as the $W_{MJO,K}$. Using model output, LS18 have shown that there is a statistically significant relationship between January–July average $W_{MJO,K}$ variance, measured by the $W_{MJO,K}$ index and the December-January-February Niño 3 index. The same relationship exists in observations, as shown in Figure 1. One caveat of Figure 1 is the relatively low statistical significance level of the regression (80%). For model results of LS18, which include more ENSO

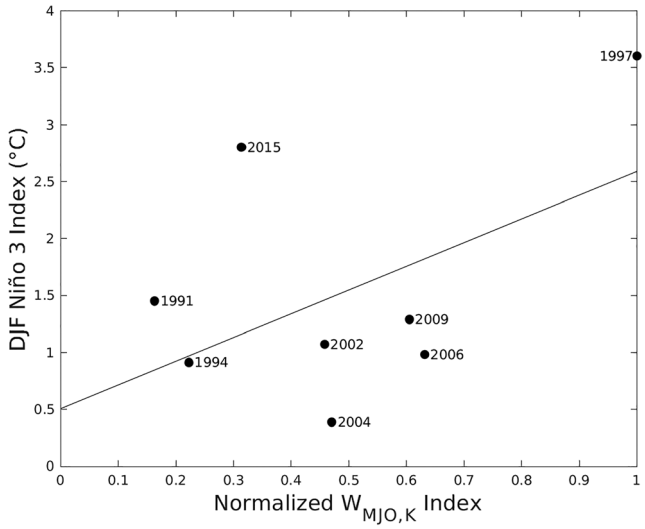

Figure 1. Scatter plot of the $W_{MJO,K}$ index averaged between January and July prior to the peak of El Niño versus the DJF average Niño 3 index. Superimposed is the linear regression of DJF average Niño 3 index on the normalized $W_{MJO,K}$ index and the El Niño year corresponding to each point. Linear regression is significant at the 80% confidence level.

samples than available from observations, the significance level is higher than in observations. We attribute the low value in observations to the small sample size available for observed El Niño events. The El Niño in 1997/1998 strongly influences this regression, while 2009/2010 and 2006/2007 show the next highest values of the $W_{MJO,K}$ index. In further discussions of the MJO influence on El Niño, these three El Niño years will be identified as those events, which are strongly influenced by the MJO.

For real-time seasonal forecasting applications, this methodology cannot be used to compute the $W_{MJO,K}$ because it requires band-pass filtering and HSVD analysis to isolate the MJO-related wind stress, $\tau_{MJO}(x, y, t)$. A surrogate method must therefore be developed. In this real-time methodology for computing $\tau_{MJO}(x, y, t)$, the first four modes of the HSVD spatial patterns (empirical orthogonal functions, EOFs) computed for observations are projected onto the unfiltered wind stress anomalies. Because these EOFs are computed for intraseasonal wind stress anomalies, they should isolate at least some portion of the variability associated with intraseasonal time scales, even if they are projected onto unfiltered anomalies. As seen in Figure 2, EOFs 1 and 2 display stronger amplitudes in the western Pacific and a lesser basin-wide influence. EOF3 shows a tripole pattern, with positive values along the western boundary north of the

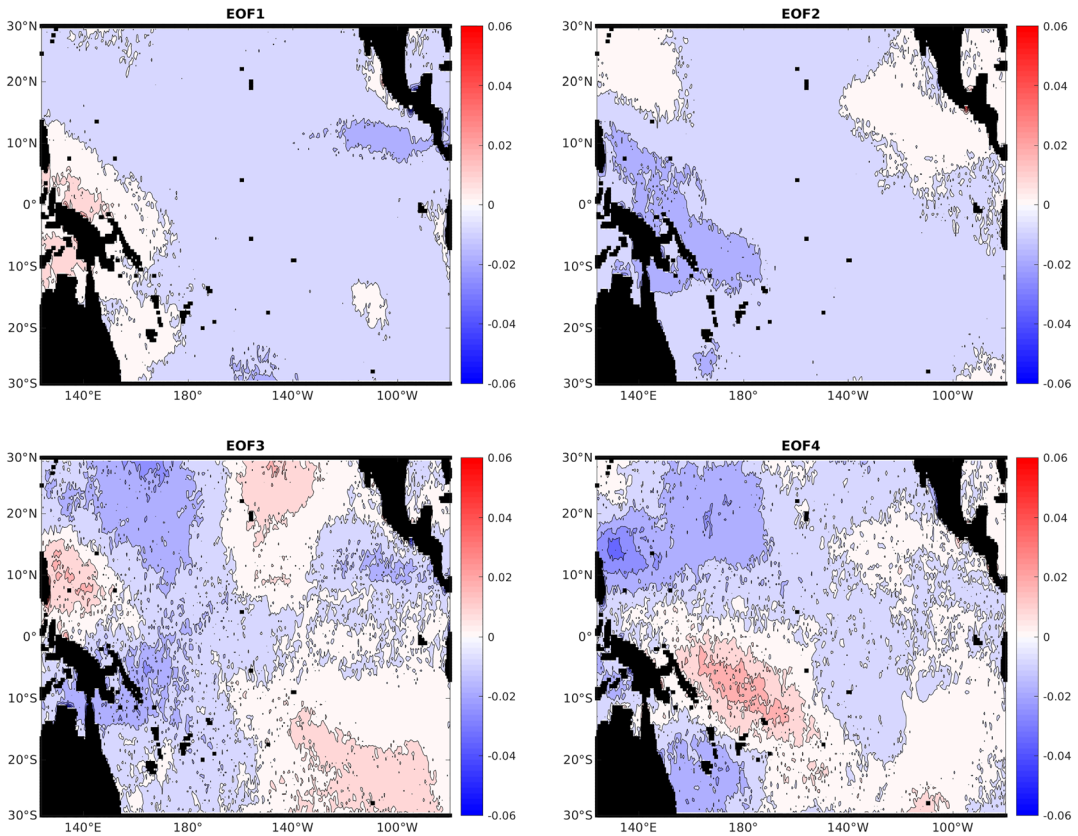

Figure 2. Amplitudes of EOFs from HSVD analysis performed on observed intraseasonally band-pass-filtered wind stress anomalies. Positive (negative) anomalies denote westerly (easterly) wind stress. EOF1 explains 31.3% of the variance in τ_{MJO}, EOF2 explains 21.5%, EOF3 explains 7.9%, and EOF4 explains 7.2%. Units are N m^{-2}.

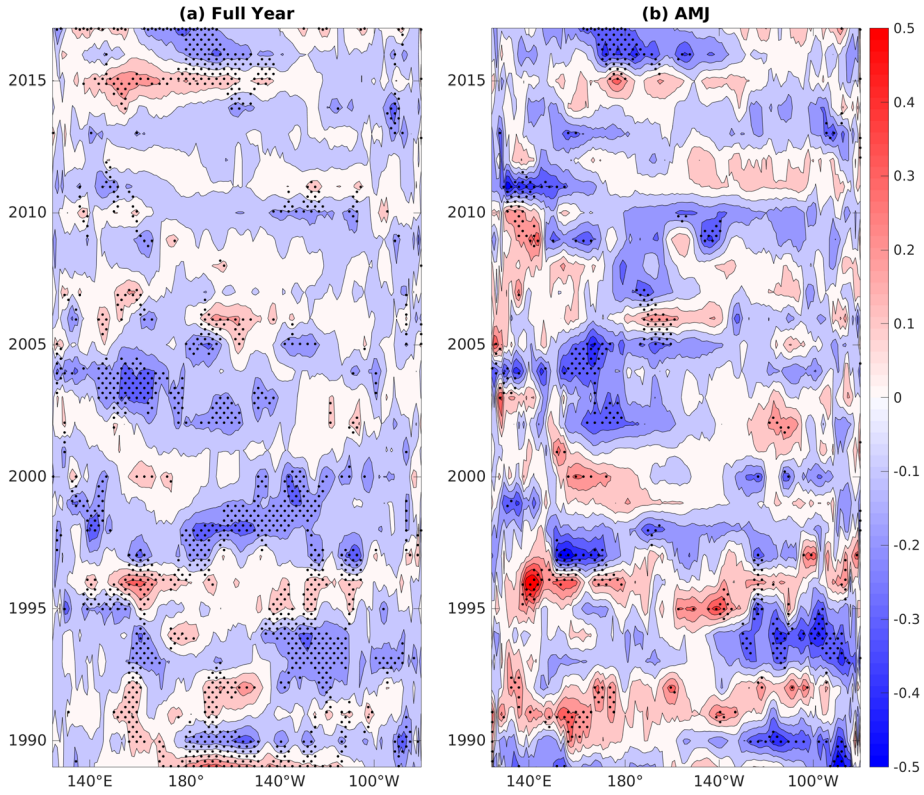

Figure 3. Hovmöller diagrams of correlation coefficients between actual $W_{MJO,K}$ and the proxy $W_{MJO,K}$. This correlation is computed for each year independently, (a) for the full year and (b) for only the April-May-June (AMJ) season. Stippling indicates statistical significance at the 95% level using a two-sided *t* test.

equator, negative values along the dateline that extend along the equator north to central America, and those eastern Pacific negative anomalies are flanked on the north and south by positive anomalies. EOF4 shows the opposite pattern for many regions when compared with EOF3, with a negative value along the western boundary north of the equator. A strong positive region extends from the coast of Papua New Guinea southeastward into the central Pacific, with the opposite sign of the values seen there in EOF3. The first two EOFs describe the familiar MJO pattern with easterlies across the Pacific with EOF2 approximately in quadrature with EOF1. According to Zhang and Gottschalck (2002) the last two modes (EOF3 and EOF4) account for the zonal shift of the MJO during El Niño events identified by Kessler (2001). The PCs corresponding to these EOFs are projected onto the unfiltered wind stress anomalies and combined, giving a proxy for $\tau_{MJO}(x, y, t)$ that can be used for real-time applications. The computation of daily Kelvin wave-related surface current requires no change for real-time applications. Combining these terms gives a proxy $W_{MJO,K}$. To compare the results of this method with the direct calculation, Figure 3 shows the correlation between the actual and proxy values of $W_{MJO,K}$ averaged between 5°S and 5°N, computed for each year and zonal grid point. In this comparison the proxy values are computed by treating observations as forecasts. There is some disagreement between these terms, and that disagreement varies on interannual time scales. Because u_K is computed the same way for each method, the difference must be due to the difference between the total wind stress anomalies and the intraseasonal anomalies. This figure shows that there are periods during which the intraseasonal wind stress anomalies are especially correlated with the total wind stress anomalies, such as 1997, 2006, and 2015. It should be expected that during these times the proxy performs better than at times when they are uncorrelated, or even anticorrelated. Because AMJ is used as the prediction period for this proxy, the correlations between the proxy and "true" method during this period are especially important. It is perhaps no coincidence that the periods of greatest correlation tend to coincide with ENSO periods previously identified as being strongly influenced by MJO (1997, 2006, and less so for 2009).

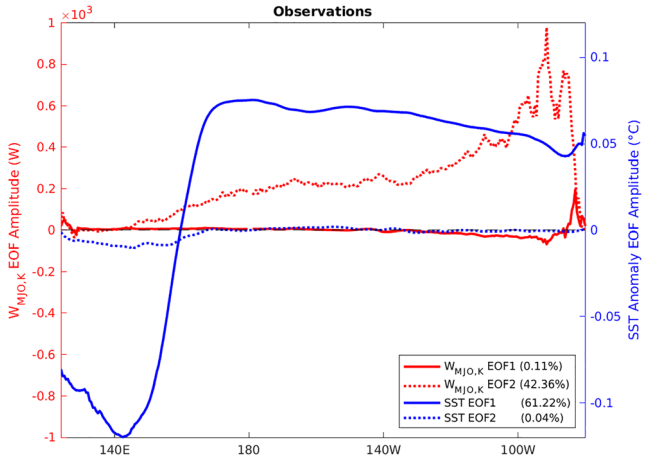

Figure 4. Multivariate EOF patterns of equatorially averaged (5°S to 5°N) $W_{MJO,K}$ (red) and SST anomalies (blue) in the tropical Pacific. Collectively, EOF1 (solid lines) explains 30.8% of the total daily variability, and EOF2 (dotted lines) explains 21.1% of the total daily variability. Included in the legend is the fraction of each EOF explained by each variable.

2.3. EOF Analysis

In LS18, El Niño years with relatively high $W_{MJO,K}$ variance in the $W_{MJO,K}$ region from January–July were defined as being strongly influenced by the MJO. Those events show the development of El Niño-like thermocline anomalies earlier in the year, stronger and more frequent downwelling Kelvin wave activity and higher peak SST amplitude than other El Niño years. However, when the $W_{MJO,K}$ index is computed for every year and used as a predictor, there is little skill in predicting El Niño events, consistent with the fact that the MJO and corresponding Kelvin wave activity occurs in varying strength irrespective of the presence of El Niño, and consistent with the idea that the MJO is not the primary initiator or driver of El Niño events.

To capture the covariability of MJO wind stress, Kelvin wave activity, and SST anomalies, the multivariate EOFs of equatorial (5°S to 5°N) average values of $W_{MJO,K}$ and SST anomalies are computed. Multivariate EOF analysis is one of the EOF-based methods (von Storch & Zwiers, 1999; Wilks, 1995) used to identify structures in geophysical data. Because of its ability to incorporate different variables with their combined variances, multivariate EOF analysis is a common method used for investigating atmosphere-ocean coupled variability (Alvera-Azcárate et al., 2007; Liang et al., 2018; Xue et al., 2000) and convectively coupled variability of the tropical atmosphere (Lin, 2013; Wheeler & Hendon, 2004). In the multivariate EOF analysis each field is normalized by its global variance to ensure an equal contribution to the variance of the total EOF (Wheeler & Hendon, 2004). After normalization, daily anomalies of meridional averaged $W_{MJO,K}$ and SST are combined into one variable that has dimensions of 2 times the number of longitudinal grid points and time. The covariance matrix is computed for the period January 1998 to 31 December 2016. Once the normalized EOF patterns have been computed, they are multiplied by the global variance of each variable to give the spatial patterns in their physical units.

The zonal structure of the leading two EOFs of the combined fields of $W_{MJO,K}$ and SST daily anomalies averaged between 5°S and 5°N are shown in Figure 4. EOF1 explains 30.8% of the daily variance and is dominated by variability in the SST anomalies. EOF2 explains 21.1% of the daily variance and is dominated by variability in $W_{MJO,K}$. The two leading EOFs are well separated according to the criterion of North et al. (1982). EOF1 is reminiscent of ENSO variability with a dipole SST structure between the western and central through eastern Pacific and is similar to the ENSO pattern found by previous studies (see for comparison Figure 1 in Roundy, 2015). In EOF2, however, $W_{MJO,K}$ EOF amplitude is very close to 0 for much of the western Pacific and acquires increasingly strong positive values in the central and eastern Pacific, indicating the importance of these regions for SST-$W_{MJO,K}$ covariability. This is consistent with Harrison and Vecchi (2001), who found that the tropical Pacific SST is generally only sensitive to thermocline variability in the central and eastern Pacific due to the relatively shallow climatological thermocline depth there. Figure 5 shows the daily PC time series, normalized by their respective standard deviations as well as the time series of monthly Niño 3.4 index values along with the nine El Niño events considered in this study (1991, 1994, 1997, 2002, 2004, 2006, 2009, 2014, and 2015). Year 2014 is included in this analysis because although the easterly wind anomalies in boreal summer and off-equatorial cool SST anomalies suppressed what was expected to be a very strong El Niño, weak El Niño conditions did develop by the end of that year (Hu & Fedorov, 2016; Min et al., 2015; Zhu et al., 2016). Variability of PC1 and Niño 3.4 agrees quite well, while PC2 is dominated by variability in $W_{MJO,K}$ on intraseasonal time scales. Highlighted in red are years identified by the $W_{MJO,K}$ index as being strongly influenced by the MJO. Interestingly, La Niña events tend to show weaker variability of PC2 than El Niño events (excepting 1998). Predictive indices have been computed using these PCs. Their derivation and results associated with them are discussed in section 3.

To approximate the multivariate PC time series for real-time forecasting applications, the spatial EOF patterns computed for observations (shown in Figure 4) are projected onto equatorially averaged SST anomalies and equatorially averaged values of the proxy $W_{MJO,K}$ described in the previous section. In each case, these

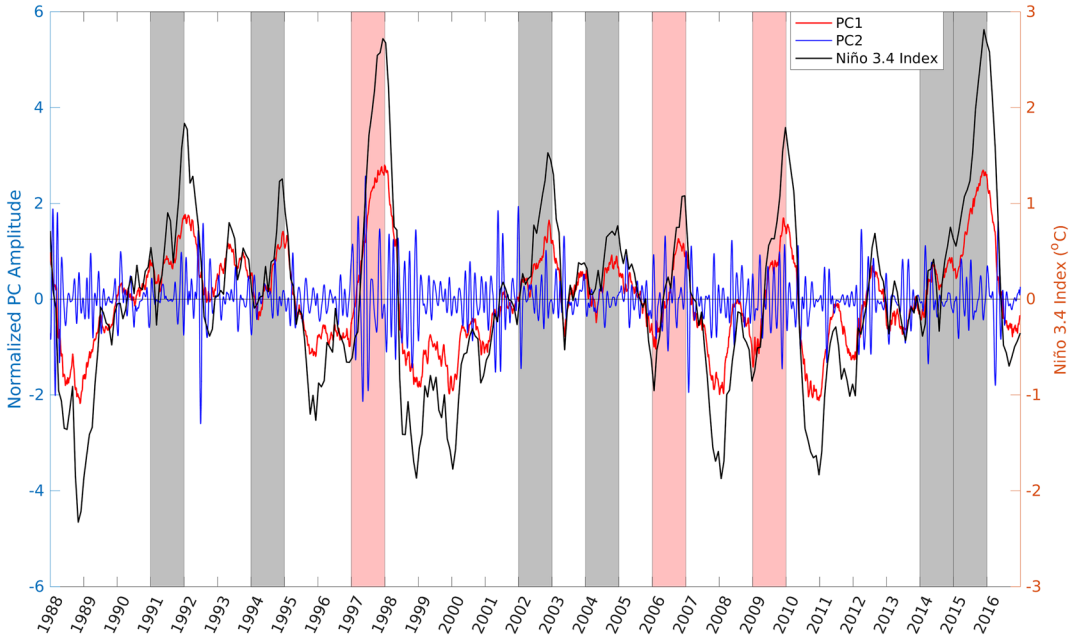

Figure 5. Normalized daily time series of PC1 (red) and PC2 (blue) from multivariate EOF analysis on equatorially averaged $W_{MJO,K}$ and daily SST anomalies. PC2 has been smoothed by a 30-day running mean filter. Monthly values of Niño 3.4 (black) are also shown to indicate that PC1 captures much of that variability. El Niño events throughout the time series are indicated by the background shading. Events that are strongly influenced by MJO by the criteria of LS18 are shaded in red ($n = 3$), while the other El Niño events ($n = 6$) are shaded in gray.

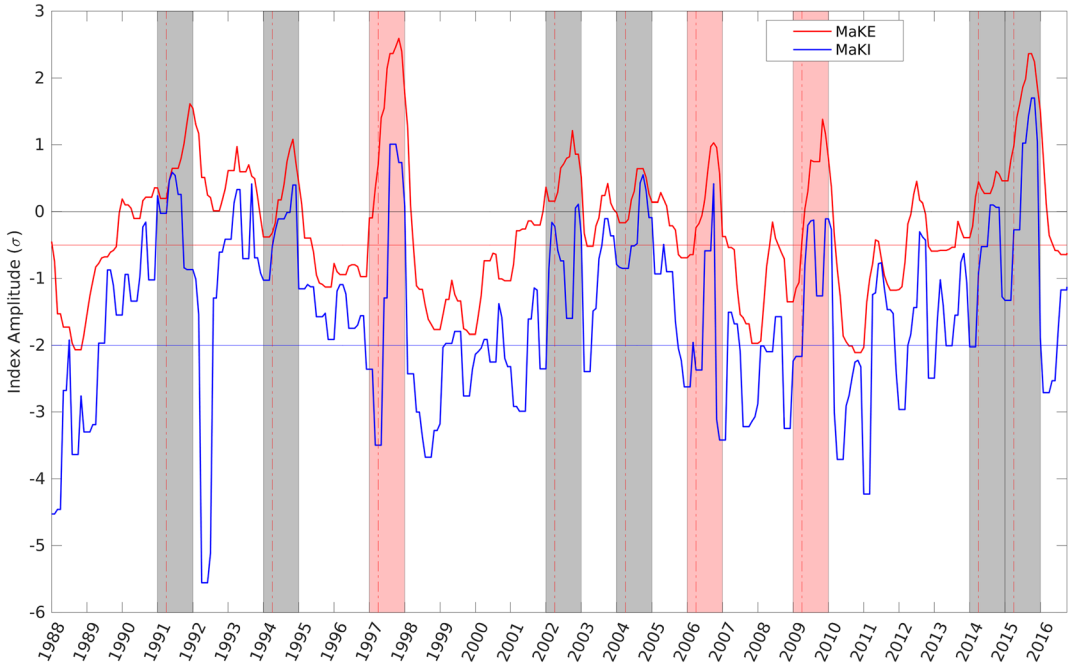

Figure 6. Time series of the *MaKE* (red) and *MaKI* (blue) indices in observations. El Niño years are highlighted by the background shading, with events that are strongly influenced by MJO highlighted in red and all other events highlighted in gray. The -0.5σ (-2σ) threshold value for *MaKE* (*MaKI*) is shown by the horizontal red (blue) line. For each El Niño year, the month of April is indicated by the vertical black line because that is the month identified as having predictive power for these indices.

Table 1
Contingency Tables for April-May-June (Top) and May-June-July (Bottom) for MaKE Used as a Predictor

		Observed			
MaKE		El Niño	Other	Total	HSS
April	El Niño	9	8	17	0.482
	Other	0	12	12	
	Total	9	20	29	
May	El Niño	9	9	18	0.431
	Other	0	11	11	
	Total	9	20	29	

Note. All nine observed El Niño events are correctly predicted. The Heidke skill scores (HSS) for each period is also shown.

equatorially averaged terms are normalized by the standard deviation of observations at each grid point. These PCs are then combined into indices and used as predictors of El Niño events in both observations and CFSv2 reforecasts.

3. Results

3.1. El Niño Predictors in Observations

A new index is then derived by combining the observational multivariate PCs described in section 2 and shown in Figure 5. This index describes the covarying nature of MJO, Kelvin wave activity, and ENSO and thus is called the MJO-Kelvin wave-ENSO (*MaKE*) index. It is defined as the minimum value of the linear combination of PC1 and |PC2| over a 90-day period:

$$MaKE(t_m) = \min_{1 < t < 90} (PC1(t_d) + |PC2(t_d)|),$$

where t_m indicates monthly frequency and t_d indicates daily frequency beginning on the first day of each month. For example, the value of *MaKE* for April is the minimum value of $PC1(t_d) + |PC2(t_d)|$ on any day between April and June. Note that *MaKE* is defined only for each month, whereas PC1 and PC2 are defined daily.

The index is intended to capture El Niño events, which are associated with positive values of PC1 (Figure 5) and negative values of wind power (Goddard & Philander, 2000; Hu et al., 2014; LS18), necessitating the absolute value of PC2 so that positive SST anomalies point in the same direction as negative deviations of wind power. Figure 6 shows the monthly time series of *MaKE* with ENSO years highlighted. To use this index as a predictor of ENSO, a threshold value of -0.5σ in April (i.e., the minimum over AMJ) is chosen to maximize prediction skill, above which a given year is more likely to result in El Niño and below which a given year is less likely to result in El Niño. When *MaKE*'s values are greater than -0.5σ, it means that either PC1 and therefore SST anomalies that are covarying with $W_{MJO,K}$ are consistently positive over this period (which would tend to suggest El Niño growth) or that negative/neutral SST anomalies are accompanied by consistently strong wind anomalies and Kelvin wave activity captured by |PC2|. The latter case could correspond to La Niña events, such as the events in 1995/1996, 2005/2006, and 2016/2017. In those cases, Niño 3.4 is near zero in AMJ, but significant amplitudes of PC2 cause *MaKE* to identify these years as El Niño events.

Tests conducted using only PC1 as a predictor showed that PC1 misses many El Niño events that have not developed strongly positive SST anomalies during AMJ. Including the influence of absolute wind power captures every El Niño and also produces more false positives. Verification using a contingency table, shown in Table 1, demonstrates the finding that $MaKE > -0.5\sigma$ has predictive skill with respect to El Niño. This metric achieves hits in April for all El Niño years (1991, 1994, 1997, 2002, 2004, 2006, 2009, 2014, and 2015; $n = 9$) and several false positives in April (1990, 1992, 1993, 1995, 2001, 2005, 2012, and 2016; $n = 8$). A similar metric using Niño 3.4 is also created for comparison. Over each 3-month period for which *MaKE* is calculated, the mean of the Niño 3.4 index is also computed. Table 2 shows the corresponding results using mean (Niño 3.4) > 0.2°C as a predictor (a threshold of 0.2°C was chosen to give the most generous prediction skill

Table 2
Contingency Tables for April-May-June (Top) and May-June-July (Bottom) for Niño 3.4 Used as a Predictor, As Well As Corresponding Heidke Skill Scores (HSS)

		Observed			
Niño 3.4		El Niño	Other	Total	HSS
April	El Niño	6	4	10	0.453
	Other	3	16	19	
	Total	9	20	29	
May	El Niño	6	4	10	0.453
	Other	3	16	19	
	Total	9	20	29	

to this predictor). Although several false positives are found, it is notable that *MaKE* correctly predicts *all* El Niño events using only data from AMJ, although it admittedly outperforms using the mean of Niño 3.4 over this period only slightly (6.4%), with Heidke skill scores (HSSs) of 0.482 and 0.453, respectively (HSS < 0 indicates a prediction worse than chance, HSS = 0 indicates a prediction equivalent to random chance, and HSS > 0 indicates the fraction of correct predictions that are beyond what is expected by random chance). When this same metric is applied to the May-June-July season, the predictive power wanes slightly, achieving an HSS of 0.431, while using the mean of Niño 3.4 over this period does not change that result.

Previous analyses using $W_{MJO,K}$ focused on identifying the characteristics of El Niño years, which are strongly influenced by the MJO (LS18; LS19), so it is natural to pursue a method for achieving this goal. The *MaKE* index does not have any skill in selecting the El Niño events influenced by the MJO. To achieve this, a second new index is computed, meant to be used in conjunction with *MaKE*. This second index should only be applied to those events predicted to be El Niño by *MaKE*, as it is of little value in differentiating between El Niño and non–El Niño events. The MJO and Kelvin wave Influence (*MaKI*) index is defined as the minimum value of the linear combination of PC1 and PC2 over a 90-day period:

$$MaKI(t_m) = \min_{1 < t < 90} (PC1(t_d) + PC2(t_d)),$$

where t_m indicates monthly frequency and t_d indicates daily frequency beginning on the first day of each month. Like the *MaKE* index, *MaKI* is defined only for each month. *MaKI* is designed to capture events when the wind power variability, which is described by PC2, dominates the MJO-ENSO covariability. Thus, while *MaKE* is designed to capture the maximum covariability between SST and wind power, *MaKI* further selects from these events those dominated by the negative wind power, which is the mechanism through which MJO affects the oceanic Kelvin waves. Because the years to which this index is applied are predicted by *MaKE* to be El Niño, the absolute value used in computing *MaKE* can be relaxed due to the fact that negative wind power can be assumed to contribute to the growth of El Niño

Table 3
Contingency Tables for April-May-June (Top) and May-June-July (Bottom) for MaKI Used as a Predictor, As Well As Corresponding Heidke Skill Scores (HSS)

		Observed			
MaKI		Strong	Other	Total	HSS
April	Strong	3	3	6	0.564
	Other	0	11	11	
	Total	3	14	17	
May	Strong	2	3	5	0.368
	Other	1	12	13	
	Total	3	15	18	

Note. It should be noted that this metric is only applied to the set of years predicted by the *MaKE* index to be El Niño events.

(Goddard & Philander, 2000; Hu et al., 2014; LS18). Figure 6 shows the monthly time series of *MaKI* with El Niño events influenced by the MJO highlighted in red.

In this case, a threshold of $MaKI < -2\sigma$ for determining whether the predicted El Niño will be strongly influenced by the MJO is also chosen to maximize prediction skill. These events are tending toward El Niño according to *MaKE*; thus, PC1 will usually be positive. For this condition to be met, PC2 must have at least one strongly negative phase that dominates PC1 enough to bring their sum below -2σ. The reasoning for only applying this index to events predicted to be El Niño should be clear: If applied to a year tending toward La Niña, many years would meet the $MaKI < -2\sigma$ criterion due to the influence of strongly negative SST anomalies on PC1. Applying this metric to the set of 17 years predicted to be El Niño in AMJ by the *MaKE* metric results in correctly identifying the three years that are strongly influenced by the MJO according to the $W_{MJO,K}$ index (1997, 2006, and 2009), as well as misidentifying three other years as being strongly influenced by the MJO (1992, 2001, and 2016). Figure 6 demonstrates that the *MaKE* index correctly predicts each El Niño (red and gray background shading) in April (indicated by the vertical black line in each El Niño year) and that the *MaKI* index correctly predicts the El Niño events, which are influenced by the MJO (red background shading). The set of years which meet both the $MaKE > -0.5\sigma$ and $MaKI < -2\sigma$ criteria in April are the El Niño years 1997, 2006, and 2009 (all identified by the $W_{MJO,K}$ index as being strongly influenced by the MJO), the ENSO-neutral years 1992 and 2001, and the La Niña year 2016. Table 3 summarizes these findings, with *MaKI* achieving an HSS of 0.564 in April when applied to the 17 years that meet the *MaKE* threshold. The MJO influence on El Niño years has been shown to be due to coherent variations between MJO wind stress and Kelvin wave activity (LS19), so lag correlations are now computed to investigate this relationship with respect to the years selected by these criteria. These lag-correlation plots can also be used to validate whether the events selected by *MaKI* as El Niño events without a link to MJO lack the coherence between MJO wind stress and oceanic Kelvin waves.

Figure 7 shows the AMJ lag correlation between the area average of τ_{MJO} in the $W_{MJO,K}$ region (3°S to 1°N, 175°E to 160°W) and the meridional average (5°S to 5°N) of Kelvin wave depth in the anomalies of the 20°C isotherm. LS19 showed that for El Niño events influenced by MJO, westerly MJO wind stress anomalies over the $W_{MJO,K}$ region tend to be preceded by upwelling Kelvin wave activity in the western Pacific (negative correlation between westerly wind stress anomaly and negative thermocline depth anomaly) and followed by downwelling Kelvin waves that propagate into the eastern Pacific (positive correlation between westerly wind stress anomaly and positive thermocline depth anomaly). Four different composites are shown, corresponding to whether the year achieves the *MaKI* threshold (-2σ) and whether that year resulted in El Niño. In each composite shown in Figure 7, $MaKE > -0.5\sigma$ in April and is therefore predicted by that metric to be an El Niño event. Figure 7a shows the composite of all years (1992, 1997, 2001, 2006, 2009, and 2016; $n = 6$) that meet the condition $MaKI < -2\sigma$, Figure 7b shows the actual El Niño years (1997, 2006, and 2009; $n = 3$) for which $MaKI < -2\sigma$, and Figure 7c shows non–El Niño years (1992, 2001, and 2016; $n = 3$) for which $MaKI < -2\sigma$. Because the years included in each of these three composites achieve the *MaKI* threshold, they are predicted by that metric to be strongly influenced by the MJO. Figure 7d shows the composite of all years (1990, 1991, 1993, 1994, 1995, 2002, 2004, 2005, 2012, 2014, and 2015; $n = 11$) for which $MaKI > -2\sigma$, and Figure 7e shows the composite of actual El Niño years (1991, 1994, 2002, 2004, 2014, and 2015; $n = 6$) for which $MaKI > -2\sigma$, and Figure 7f shows non–El Niño years (1990, 1993, 1995, 2005, and 2012; $n = 5$) for which $MaKI > -2\sigma$. Because the years included in each of these three composites (d–f) do not achieve the *MaKI* threshold, they are predicted by that metric not to be influenced by MJO wind forcing. Figures 7b and 7e show a composite of a subset of years included in (a) and (d), which, in reality, evolve into El Niño. The El Niño years in Figures 7b and 7e show essentially the same spatial structures as their counterparts in Figures 7a and 7d, but with stronger amplitudes. An exception to this is the slightly stronger eastward propagation seen in (e) as compared to (d), which looks more like a standing wave. This eastward propagation is also not present in (f), which is almost identical to (d). This result contrasts with previous findings of Roundy and Kiladis (2006) who showed a decrease in Kelvin wave phase speeds as the ocean state evolves toward El Niño, though that study investigated the summer and autumn prior to El Niño, and not AMJ as shown here. MJO wind stress is followed by Kelvin wave depth of opposite sign when *MaKI* does not meet the -2σ threshold (Figures 7d–7f), indicating MJO wind stress that is out of phase with Kelvin wave activity, consistent with the findings of LS19. Curiously, Figures 7d–7f also show the development of positive correlations at negative lags, indicating MJO wind stress is preceded by Kelvin wave activity of the same sign.

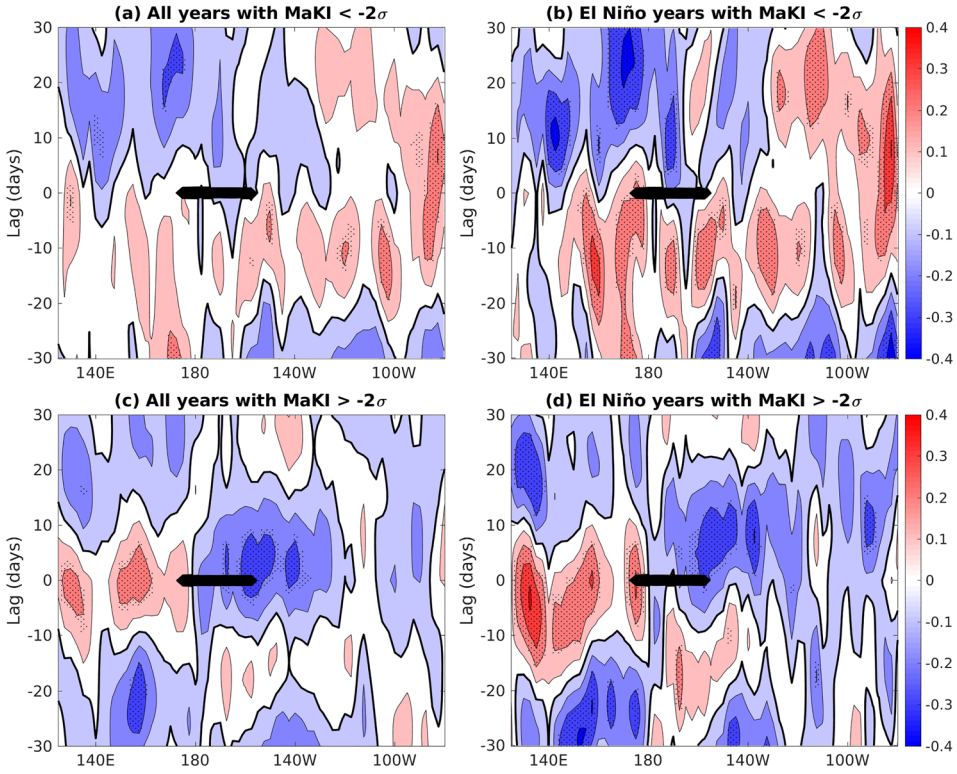

Figure 7. Composites of AMJ lag correlation between MJO wind stress in the $W_{MJO,K}$ region and equatorially averaged Kelvin wave component of thermocline depth anomaly. The sign convention is such that a downwelling Kelvin wave (positive thermocline depth anomaly) would be correlated with a westerly MJO wind stress anomaly. Each composite includes only years with meet the *MaKE* threshold. Shown are composites of (a) all years that also meet the *MaKI* index threshold (1992, 1997, 2001, 2006, 2009, and 2016; $n = 6$), (b) El Niño years that meet the *MaKI* threshold (1997, 2006, and 2009; $n = 3$), (c) non–El Niño years that meet the *MaKI* threshold (1992, 2001, and 2016; $n = 3$), (d) all years that do not meet the *MaKI* threshold (1990, 1991, 1993, 1994, 1995, 2002, 2004, 2005, 2012, 2014, and 2015; $n = 11$), (e) El Niño years that do not meet the *MaKI* threshold (1991, 1994, 2002, 2004, 2014, and 2015; $n = 6$), and (f) non–El Niño years that do not meet the *MaKI* threshold (1990, 1993, 1995, 2005, and 2012; $n = 5$). The zonal extent of the $W_{MJO,K}$ region is blacked out. Positive (negative) lags indicate MJO wind stress leading (lagging) Kelvin waves. Stippling indicates statistical significance at the 95% level.

It seems that in these composites, MJO wind stress in this region in AMJ works to reverse Kelvin wave activity. In the $MaKI < -2\sigma$ composites (Figures 7a–7c), coherent phasing between MJO wind stress and Kelvin wave activity throughout the basin is seen at negative lags (albeit weaker amplitudes are seen in panel c), significantly so in years resulting in El Niño (Figure 7b). At positive lags, the western and central Pacific Kelvin wave depth is anticorrelated with MJO wind stress in Figure 7b, while the eastern Pacific is positively correlated. Figure 7c shows similar spatial structure and smaller amplitude compared to (a) and (b) in the western and central Pacific but very little correlation in the eastern Pacific at positive lags except at the eastern boundary. The composites of events selected by *MaKI* show coherence between the $W_{MJO,K}$ region and the eastern Pacific at positive lags, particularly in true El Niño years, suggesting that this index is effectively capturing the source of MJO influence on ENSO found in LS19. Figures 7d–7f are reminiscent of the composite of El Niño events in LS19 without a relationship to MJO wind forcing.

3.2. ENSO Forecast in CFSv2

The metrics that have been applied to observations were also applied to the PCs (described in section 2.1) computed from CFSv2 reforecasts of each year in the period 1980–2014. The PCs and indices are computed for each of the five ensemble members using the proxy method described in the last paragraph of section 2.2. Table 4 shows the contingency table using the ensemble mean of *MaKE* as a predictor. The same threshold value of -0.5σ as in observations is used for prediction of El Niño events by the model. Table 5 shows the contingency table resulting from using the ensemble mean Niño 3.4 as a predictor. The threshold value of

Table 4
MaKE Contingency Table as Applied to CFSv2 Reforecasts of Each Year Between 1980 and 2014

		Observed			HSS
MaKE		El Niño	Other	Total	
CFSv2	El Niño	9	9	18	
	Other	2	15	17	0.378
	Total	11	24	35	

Note. The Heidke skill score is shown.

mean (Niño 3.4) > 0.2°C in AMJ is used for prediction of El Niño events by CFSv2, as was done for observations. Nine of the 11 El Niño events observed between 1980 and 2014 are correctly predicted by *MaKE*, as well as 9 false positives, while only 5 El Niño events are captured using the mean of Niño 3.4 metric, with 9 false positives as well. The skill score of the Niño 3.4 predictor measured by HSS is 0.074, barely outperforming a chance prediction and is surpassed considerably by the *MaKE* predictor, which achieves an HSS of 0.378. In the CFSv2 reforecasts, both *MaKE* and Niño3.4 predictors have a lower forecast skill than their counterparts computed in observations, providing some hope for improving the Niño 3.4 prediction.

To explore the probabilistic forecast skill of the CFSv2 reforecasts using *MaKE* and compare it to that based on Niño 3.4, the receiver operating characteristic (ROC) plots associated with Tables 4 and 5 are shown in Figure 8 for each ensemble member and predictor. On this ROC plot, any point above the red dotted line outperforms chance, while any point below does not. Each ensemble member for both predictors outperform chance, in agreement with the positive HSS values from the ensemble mean, but the distance from the center line in the group of points representing the *MaKE* metric for each ensemble member is considerably larger than for the group of points representing the mean of Niño 3.4 metric for each ensemble member. For Niño 3.4, all members achieve a true positive rate (TPR) of 45%, with two members having a false positive rate (FPR) of 37.5% and three having an FPR of 33.3%.

The mean of Niño 3.4 metric suffers a far more dramatic loss of skill in predicting El Niño than does the metric based on *MaKE*. A possible explanation for this is an insufficient coupling between oceanic and atmospheric processes in CFSv2, such that the wind variability does not accurately influence the ocean (though the state of the ocean may still strongly influence the atmosphere). This would result in inaccuracies in Niño 3.4 that can be compensated by also directly quantifying the impact of MJO wind variability on the ocean surface, thus resulting in a more accurate predictor of El Niño events. These results indicate that including the influence of $W_{MJO,K}$ can be a significant source of ENSO predictability as early as April in CFSv2 forecasts.

The *MaKI* metric to identify El Niño events that are strongly influenced by the MJO is also applied to the CFSv2 reforecast years predicted by the *MaKE* metric to be El Niño years. Unlike for observations, this metric does not capture every El Niño year, specifically missing 1986/1987 and 2009/2010 (the latter of which has been identified as strongly influenced by the MJO in observations). Furthermore, because DASCAT satellite data are only available going back to 1987, it is possible that years between 1980 and 1987 could have included El Niño events that were strongly influenced by the MJO, which would provide more targets for *MaKI* to forecast. As a counterexample, the 1982/1983 El Niño event is known to be of strong amplitude, but little MJO activity was observed in the year prior to that event (Tang & Yu, 2008). It should therefore be expected that *MaKI* does not predict strong influence by the MJO on that event. Indeed, *MaKI* attains a value of -0.54σ in the CFSv2 reforecast of 1982, and so does not achieve the threshold value of -2σ. Because so few targets are available for CFSv2, the best possible outcome for applying this metric to these CFSv2 reforecasts would be to correctly predict strong MJO influence prior to the El Niño events in 1997 (-0.81σ) and 2006 (-1.03σ). No years meet the threshold of -2σ, though the years which come closest are 2006 and 2012 (-1.59σ, ENSO-neutral).

Table 5
Niño 3.4 Contingency Table as Applied to CFSv2 Reforecasts of Each Year Between 1980 and 2014

		Observed			HSS
Niño 3.4		El Niño	Other	Total	
CFSv2	El Niño	5	9	14	
	Other	6	15	21	0.074
	Total	11	24	35	

Note. The Heidke skill score of 0.074 is shown, indicating this predictor only slightly outperforms random chance.

These results suggest that El Niño simulated by CFSv2 is driven by ocean dynamics and atmospheric forcing associated with the MJO simulated by the model does not play a role in the formation of El Niño. To demonstrate the lack of coherence between MJO wind stress and SST anomalies in CFSv2 forecasts, Hovmöller diagrams for the ensemble average, equatorial average (5°S to 5°N) zonal MJO wind stress, total wind stress anomalies, and SST anomalies over the CFSv2 reforecast of 1997 are compared in Figure 9. In this figure, the anomalies are defined as deviations from the daily climatology computed over all CFSv2 reforecasts. Despite the significant periods and regions over which the MJO wind stress and the total wind stress anomalies are easterly, the SST anomalies show a quite

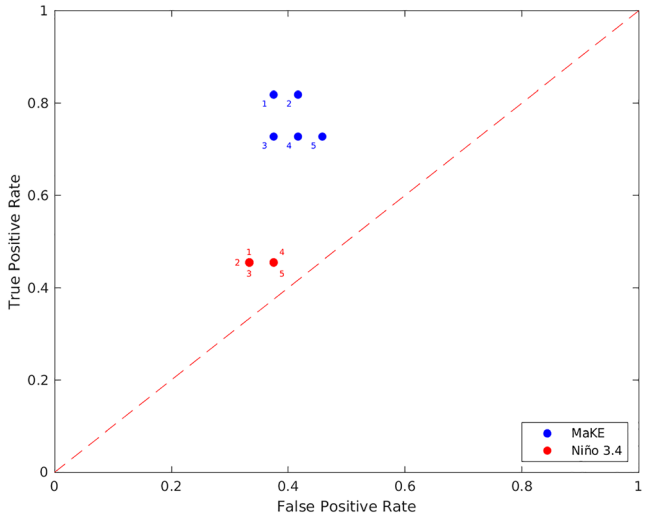

Figure 8. Receiver operating characteristic (ROC) plots for each ensemble member of the CFSv2 reforecasts. ROC plots compare the true positive rate and false positive rate, with any points above the center line outperforming chance. Note that the distance between each point and the center line for *MaKE* (blue) is considerably larger than for Niño 3.4 (red). The numbered labels indicate the ensemble members represented by each point.

uniform growth of positive anomalies in the central and eastern Pacific after May. The period of negative SST anomalies that emerges in the eastern Pacific in April is accompanied by westerly MJO winds, counter to what should be expected, though there are easterlies in the total wind stress daily anomalies in the central/eastern Pacific during this period. These easterly anomalies drive upwelling consistent with the cool SST anomalies during April in this region. Notable periods of easterly anomalies in the total wind stress field in this same region occur in May and June as well, though positive SST anomalies continue to grow during these periods despite the easterlies (indeed, the extensive period of easterly wind stress anomalies in June is accompanied by some of the most rapid SST growth of the three months). One possible explanation for the weak ocean-atmosphere interactions in CFSv2 could be the shortcomings in the convective parameterization scheme. For example, Wu et al. (2007) showed that in a GCM the MJO, wind stress anomalies, and SST growth became closely associated when the convection scheme was modified.

The fact that *MaKE* performs as well as it does and *MaKI* has no skill could be explained by the presence of westerly wind bursts, which also play a significant role in ENSO formation (Hu et al., 2014). In the method for computing the proxy τ_{MJO}variability associated with westerly wind bursts is not removed because daily anomalies are not filtered. While the presence of westerly wind bursts can act as a booster for *MaKE*, it can downgrade the accuracy of *MaKI*. These results imply that the forecast skill of El Niño can be improved by using other metrics than Niño indices and further improvements in the skill can be achieved by improving the air-sea coupling of the model. Additional information provided by the *MaKI* index could be used to predict some features of El Niño events such as intensity and flavor (not shown here).

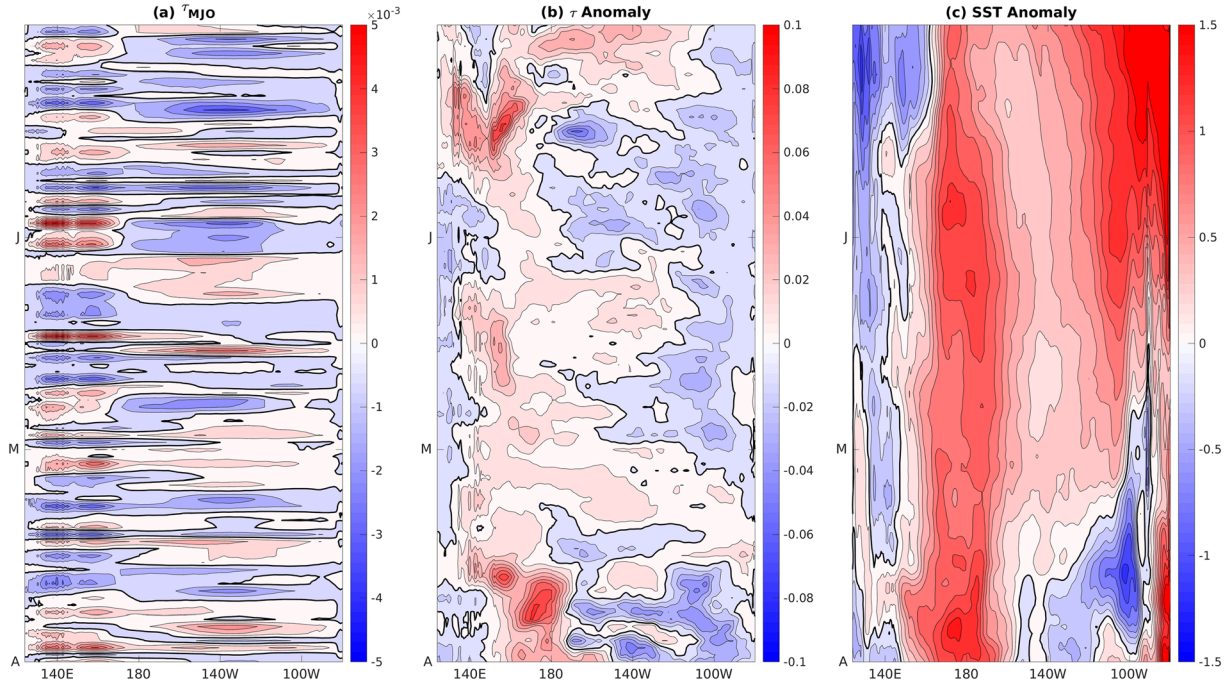

Figure 9. Hovmöller diagram of ensemble average, equatorially averaged (5°S to 5°N) zonal (a) MJO wind stress, (b) total wind stress daily anomaly, and (c) SST anomaly in the CFSv2 forecast of 1997, initialized in April. Units of wind stress are N m^{-2}, and units of SST anomaly are °C.

4. Conclusion

This study uses the covariability of MJO wind stress with oceanic Kelvin waves captured by $W_{MJO,K}$ and SST anomalies to construct a diagnostic framework for El Niño events and applies the diagnostic to an ensemble of seasonal reforecasts with the CFSv2 model. The framework consists of two indices derived from the multivariate EOF analysis of $W_{MJO,K}$ and SST daily anomalies over the domain between 3°S to 1°N and 175°E to 160°W. The first index, *MaKE*, captures years in which SSTs are either consistently above normal or, if not, are compensated by strong wind power associated with coincident MJO and Kelvin wave activity. This index correctly predicts every El Niño using data from AMJ observations. While it does predict more false positives than using a metric based on Niño 3.4, it outperforms that metric according to HSS, albeit slightly. The second index, *MaKI*, is recommended to be used only for those years predicted to be El Niño by *MaKE*. This index correctly predicts the three El Niño events that are strongly influenced by the MJO (1997, 2006, and 2009). The relationship between these El Niño events and the MJO was established using the $W_{MJO,K}$ index (LS18) calculated for all El Niño events within the observational data set considered here (Figure 1). *MaKI* captures the coherence between the MJO wind stress in the tropical central Pacific and Kelvin wave activity in the eastern Pacific identified by LS19 as the driving mechanism of the MJO-El Niño interaction. Lagged correlation plots of El Niño events stratified according to *MaKI* threshold show a coherence (decoherence) between MJO wind stress in the tropical central Pacific and Kelvin wave activity in the eastern Pacific at positive lags in composites of events which achieve (do not achieve) the *MaKI* threshold.

When these metrics are computed for the 3-month CFSv2 reforecasts initialized in early April, the *MaKE* index has a much higher prediction score than the Niño 3.4. However, the *MaKI* index is markedly less successful, with no years achieving the threshold for a successful prediction. One can speculate that *MaKE* can predict El Niño due to CFSv2 capturing the first leg of atmosphere-ocean interactions in the Pacific Ocean, namely, the ocean's influence on the winds. As the ocean evolves toward an El Niño state, *MaKE* captures the enhanced wind anomalies, which, in observations, tend to reinforce that state. In CFSv2, however, the forcing from the atmosphere to the ocean is not consistent with observations; thus, *MaKI* fails to predict the MJO influence because this metric depends on coherence between MJO winds and Kelvin wave activity.

This study exploits the MJO-ENSO relationship to develop metrics, which are shown to have skill in predicting El Niño events and the influence of MJO wind stress on the development of those events. These indices provide a holistic proxy for the MJO influence on the development of El Niño. Future work could include extending this analysis to the presatellite observational period from 1958–1980, which have already been reforecasted in CFSv2 (Huang et al., 2017, 2019). Evaluation of these indices could also be carried out using seasonal forecast models with a better representation of MJO. In CFSv2 the forecast errors of MJO grow as lead time increases and the growth is faster than in the European Centre for Medium-Range Weather Forecasts (ECMWF) prediction system (Kim et al., 2014). With further development of these indices, they could be applied to ENSO forecasts to predict events and to quantify the MJO influence on those events.

Data Availability Statement

QSCAT data are deposited in the NCEI database (https://www.ncdc.noaa.gov/data-access/marineocean-data/blended-global/blended-sea-winds). DASCAT data are deposited online (http://apdrc.soest.hawaii.edu/datadoc/ascat.php). GODAS data are deposited online (https://cfs.ncep.noaa.gov/cfs/godas/pentad/). CFSv2 data can be downloaded from the website (ftp://cola.gmu.edu/pub/stan/CFSv2).

Acknowledgments

This work was supported by U.S. NOAA Grants NA12NWS4680022 and NA20OAR4590316. The authors thank two anonymous reviwers and the editor for their constructive comments on an earlier version of this manuscript.

References

Alvera-Azcárate, A., Beckers, M. -M., & Weisberg, R. H. (2007). Multivariate reconstruction of missing data in sea surface temperature, chlorophyll, and wind satellite fields. *Journal of Geophysical Research*, *112*, C03008. https://doi.org/10.1029/2006JC003660

Batstone, C., & Hendon, H. H. (2005). Characteristics of stochastic variability associated with ENSO and the role of the MJO. *Journal of Climate*, *18*(11), 1773–1789. https://doi.org/10.1175/JCLI3374.1

Bentamy, A., & Fillon, D. C. (2012). Gridded surface wind fields from Metop/ASCAT measurements. *International Journal of Remote Sensing*, *33*(6), 1729–1754. https://doi.org/10.1080/01431161.2011.600348

Brown, J. N., & Fedorov, A. V. (2010). How much energy is transferred from the winds to the thermocline on ENSO time scales? *Journal of Climate*, *23*(6), 1563–1580. https://doi.org/10.1175/2009JCLI2914.1

Brown, J. N., Fedorov, A. V., & Guilyardi, E. (2011). How well do coupled models replicate ocean energetics relevant to ENSO? *Climate Dynamics*, *36*(11–12), 2147–2158. https://doi.org/10.1007/s00382-010-0926-8

Capodonti, A., Sardeshmukh, P. D., & Ricciardulli, L. (2018). The nature of the stochastic wind forcing of ENSO. *Journal of Climate*, *31*, 8081–8099.

Cravatte, S., Boulanger, J. P., & Picaut, J. (2004). Reflection of intraseasonal equatorial Rossby waves at the western boundary of the Pacific Ocean. *Geophysical Research Letters*, *31*, L10301. https://doi.org/10.1029/2004GL019679

Enfield, D. B. (1987). The intraseasonal oscillation in eastern Pacific sea levels: How is it forced? *Journal of Physical Oceanography*, *17*(11), 1860–1876. https://doi.org/10.1175/1520-0485(1987)017<1860:TIOIEP>2.0.CO;2

Fedorov, A. V. (2002). The response of the coupled tropical ocean-atmosphere to westerly wind bursts. *Quarterly Journal of the Royal Meteorological Society*, *128*(579), 1–23. https://doi.org/10.1002/qj.200212857901

Fedorov, A. V., Harper, S. L., Philander, S. G., Winter, B., & Wittenberg, A. (2003). How predictable is El Niño? *Bulletin of the American Meteorological Society*, *84*(7), 911–920. https://doi.org/10.1175/BAMS-84-7-911

Giese, B. S., & Ray, S. (2011). E Niño variability in simple ocean data assimilation (SODA). *Journal of Geophysical Research*, *116*, C02024. https://doi.org/10.1029/2010JC006695

Goddard, L., & Philander, S. G. (2000). The energetics of El Niño and La Niña. *Journal of Climate*, *13*(9), 1496–1516. https://doi.org/10.1175/1520-0442(2000)013<1496:TEOENO>2.0.CO;2

Harrison, D. E., & Vecchi, G. A. (2001). El Niño and La Niña—Equatorial Pacific thermocline depth and sea surface temperature anomalies, 1986–98. *Geophysical Research Letters*, *28*(6), 1051–1054. https://doi.org/10.1029/1999GL011307

Hendon, H., Zhang, C. D., & Glick, J. D. (1999). Interannual variation of the Madden-Julian oscillation during austral summer. *Journal of Climate*, *12*(8), 2538–2550. https://doi.org/10.1175/1520-0442(1999)012<2538:IVOTMJ>2.0.CO;2

Hendon, H. H., Liebmann, B., & Glick, J. D. (1998). Oceanic Kelvin waves and the Madden-Julian oscillation. *Journal of the Atmospheric Sciences*, *55*, 88–101. https://doi.org/10.1175/1520-0469(1998)055<0088:OKWATM>2.0.CO;2

Hendon, H. H., Wheeler, M. C., & Zhang, C. (2007). Seasonal dependence of the MJO-ENSO relationship. *Journal of Climate*, *20*(3), 531–543. https://doi.org/10.1175/JCLI4003.1

Hu, S., & Fedorov, A. V. (2016). Exceptionally strong easterly wind burst stalling El Niño of 2014. *Proceedings of the National Academy of Sciences U. S. A*, *113*, 2005–2010. https://doi.org/10.1073/pnas.1514182113

Hu, S., Fedorov, A. V., Lengaigne, M., & Guilyardi, E. (2014). The impact of westerly wind bursts on the diversity and predictability of El Niño events: An ocean energetics perspective: Hu et al.: WWB and ENSO diversity: Energetics view. *Geophysical Research Letters*, *41*, 4654–4663. https://doi.org/10.1002/2014GL059573

Huang, B., Shin, C.-S., & Kumar, A. (2019). Predictive skill and predictable patterns of the US seasonal precipitation in CFSv2 reforecasts of sixty years (1958–2017). *Journal of Climate*, *32*(24), 8603–8637. https://doi.org/10.1175/JCLI-D-19-0230.1

Huang, B., Shin, C.-S., Shukla, J., Marx, L., Balmaseda, M. A., Halder, S., et al. (2017). Reforecasting the ENSO events in the past 57 years (1958–2014). *Journal of Climate*, *30*(19), 7669–7693. https://doi.org/10.1175/JCLI-D-16-0642.1

Jin, E. K., Kinter, J. L. III, Wang, B., Park, C. -K., Kang, I. -S., Kirtman, B. P., et al. (2008). Current status of ENSO prediction skill in coupled ocean-atmosphere models. *Climate Dynamics*, *31*(6), 647–664. https://doi.org/10.1007/s00382-008-0397-3

Kanamitsu, M., Ebisuzaki, W., Woollen, J., Yang, S.-K., Hnilo, J. J., Fiorino, M., & Potter, G. L. (2002). NCEP–DOE AMIP-II reanalysis (R-2). *Bulletin of the American Meteorological Society*, *83*(11), 1631–1644. https://doi.org/10.1175/BAMS-83-11-1631

Kessler, W., Mcphaden, M., & Weickmann, K. (1995). Forcing of intraseasonal Kelvin waves in the equatorial Pacific. *Journal of Geophysical Research*, *100*(C6), 10,613–10,631. https://doi.org/10.1029/95JC00382

Kessler, W. S. (2001). EOF representations of the Madden-Julian oscillation and its connection with ENSO. *Journal of Climate*, *14*(13), 3055–3061. https://doi.org/10.1175/1520-0442(2001)014<3055:EROTMJ>2.0.CO;2

Kim, H.-M., Webster, P. J., Toma, V. E., & Kim, D. (2014). Predictability and prediction skill of the MJO in two operational forecasting systems. *Journal of Climate*, *27*(14), 5364–5378. https://doi.org/10.1175/JCLI-D-13-00480.1

Kim, W., Yeh, S.-W., Kim, J.-H., Kug, J.-S., & Kwon, M. (2011). The unique 2009–2010 El Niño event: A fast phase transition of warm pool El Niño to La Niña. *Geophysical Research Letters*, *38*, L15809. https://doi.org/10.1029/2011GL048521

Kirtman, B. P. (1997). Oceanic Rossby wave dynamics and the ENSO period in a coupled model. *Journal of Climate*, *10*(7), 1690–1704. https://doi.org/10.1175/1520-0442(1997)010<1690:ORWDAT>2.0.CO;2

Li, L., Jiang, X., Chahine, M. T., Wang, J., & Yung, Y. L. (2011). The mechanical energies of the global atmosphere in El Niño and La Niña years. *Journal of the Atmospheric Sciences*, *68*(12), 3072–3078. https://doi.org/10.1175/JAS-D-11-072.1

Lian, T., Chen, D., Tang, Y., & Wu, Q. (2014). Effects of westerly wind bursts on El Niño: A new perspective. *Geophysical Research Letters*, *41*, 3522–3527. https://doi.org/10.1002/2014GL059989

Liang, Y. -C., Mazloff, M. R., Rosso, I., Fang, S. -W., & Yu, Y. -Y. (2018). A multi-variate empirical orthogonal function method to construct nitrate maps in the Southern Ocean. *Journal of Atmospheric and Oceanic Technology*, *35*(7), 1505–1519. https://doi.org/10.1175/JTECH-D-18-0018.1

Lin, H. (2013). Monitoring and predicting the intraseasonal variability of the East Asian-Western North Pacific summer monsoon. *Monthly Weather Review*, *141*, 1124–1138. https://doi.org/10.1175/MWR-D-12-00087.1

Lybarger, N. D., & Stan, C. (2018). The effect of the MJO on the energetics of El Niño. *Climate Dynamics*, *51*(7–8), 2825–2839. https://doi.org/10.1007/s00382-017-4047-5

Lybarger, N. D., & Stan, C. (2019). Revisiting MJO, Kelvin waves, and El Niño relationships using a simple ocean model. *Climate Dynamics*, *53*(9–10), 6363–6377. https://doi.org/10.1007/s00382-019-04936-5

Masuda, S., Matthews, J. P., Ishikawa, Y., Mochizuki, T., Tanaka, Y., & Awaji, T. (2015). A new approach to El Niño prediction beyond the spring season. *Scientific Reports*, *5*(1), 16782. https://doi.org/10.1038/srep16782

McPhaden, M. J. (1999). Genesis and evolution of the 1997–98 El Niño. *Science*, *283*(5404), 950–954. https://doi.org/10.1126/science.283.5404.950

McPhaden, M. J., Zhang, X., Hendon, H. H., & Wheeler, M. C. (2006). Large scale dynamics and MJO forcing of ENSO variability. *Geophysical Research Letters*, *33*, L16702. https://doi.org/10.1029/2006GL026786

Min, Q., Su, J., Zhang, R., & Rong, X. (2015). What hindered the El Niño pattern in 2014? *Geophysical Research Letters*, *42*, 6762–6770. https://doi.org/10.1002/2015GL064899

Nishida, T., Kitakado, T., Matsuura, H., & Wang, S.-P. (2011). Validation of the Global Ocean Data Assimilation System (GODAS) data in the NOAA National Centre for Environmental System (NCEP) by theory, comparative studies, applications and sea truth. IOTC 9th WPB meeting, Victoria, Seychelles.

North, G. R., Bell, T. L., Calahan, R. F., & Moeng, F. G. (1982). Sampling errors in the estimation of empirical orthogonal functions. *Monthly Weather Review*, *110*, 699–706.

Peng, G., Zhang, H.-M., Frank, H. P., Bidlot, J.-R., Higaki, M., Stevens, S., & Hankins, W. R. (2013). Evaluation of various surface wind products with OceanSITES buoy measurements. *Weather and Forecasting*, *28*(6), 1281–1303. https://doi.org/10.1175/WAF-D-12-00086.1

Roundy, P. E. (2015). On the interpretation of EOF analysis of ENSO, atmospheric Kelvin waves, and the MJO. *Journal of Climate*, *28*, 1148–1165. https://doi.org/10.1175/JCLI-D-14-00398.1

Roundy, P. E., & Kiladis, G. N. (2006). Observed relationships between oceanic kelvin waves and atmospheric forcing. *Journal of Climate*, *19*(20), 5253–5272. https://doi.org/10.1175/JCLI3893.1

Rui, H., & Wang, B. (1990). Development characteristics and dynamic structure of tropical intraseasonal convection anomalies. *Journal of the Atmospheric Sciences*, *47*(3), 357–379. https://doi.org/10.1175/1520-0469(1990)047<0357:DCADSO>2.0.CO;2

Saha, S., Moorthi, S., Wu, X., Wang, J., Nadiga, S., Tripp, P., et al. (2014). The NCEP Climate Forecast System Version 2. *Journal of Climate*, *27*(6), 2185–2208. https://doi.org/10.1175/JCLI-D-12-00823.1

Saha, S., Nadiga, S., Thiaw, C., Wang, J., Wang, W., Zhang, Q., et al. (2006). The NCEP climate forecast system. *Journal of Climate*, *19*(15), 3483–3517. https://doi.org/10.1175/JCLI3812.1

Slingo, J. M., Rowell, D. P., Sperber, K. R., & Nortley, E. (1999). On the predictability of the interannual behaviour of the Madden-Julian Oscillation and its relationship with El Niño. *Quarterly Journal of the Royal Meteorological Society*, *125*(554), 583–609. https://doi.org/10.1002/qj.49712555411

Spall, M. A., & Pedlosky, J. (2005). Reflection and transmission of equatorial Rossby waves. *Journal of Physical Oceanography*, *35*(3), 363–373. https://doi.org/10.1175/JPO-2691.1

Tang, Y., & Yu, B. (2008). MJO and its relationship to ENSO. *Journal of Geophysical Research*, *113*, D14106. https://doi.org/10.1029/2007JD009230

von Storch, H., & Zwiers, F. W. (1999). *Statistical analysis in climate research* (p. 484). Cambridge: Cambridge University Press.

Waliser, D., & Coauthors (2009). MJO diagnostics. *Journal of Climate*, *22*(11), 3006–3030. https://doi.org/10.1175/2008JCLI2731.1

Wang, C., Deser, C., Yu, J.-Y., DiNezio, P., & Clement, A. (2017). El Niño and Southern Oscillation (ENSO): A review. In P. W. Glynn, D. P. Manzello, I. C. Enochs (Eds.), *Coral reefs of the eastern tropical Pacific* (Vol. 8, pp. 85–106). Netherlands: Springer.

Wheeler, M. C., & Hendon, H. H. (2004). An all-season real-time multivariate MJO index: Development of an index for monitoring and prediction. *Monthly Weather Review*, *132*(8), 1917–1932. https://doi.org/10.1175/1520-0493(2004)132<1917:AARMMI>2.0.CO;2

Wilks, D. S. (1995). *Statistical methods in atmospheric sciences* (p. 467). New York: Academic Press.

Wu, X., Deng, L., Song, X., Vettoretti, G., Peltier, W. R., & Zhang, G. J. (2007). Impact of a modified convective scheme on the Madden-Julian Oscillation and El Niño–Southern Oscillation in a coupled climate model. *Geophysical Research Letters*, *34*, L16823. https://doi.org/10.1029/2007GL030637

Xue, Y., Leetmaa, Y. A., & Ji, M. (2000). ENSO prediction with Markov models: The impact of sea level. *Journal of Climate*, *13*(4), 849–871. https://doi.org/10.1175/1520-0442(2000)013<0849:EPWMMT>2.0CO;2

Zhang, C. (2005). Madden-Julian Oscillation. *Reviews of Geophysics*, *43*, RG2003. https://doi.org/10.1029/2004RG000158

Zhang, C., & Dong, M. (2004). Seasonality in the Madden-Julian Oscillation. *Journal of Climate*, *17*(16), 3169–3180. https://doi.org/10.1175/1520-0442(2004)017<3169:SITMO>2.0.CO;2

Zhang, C., & Gottschalck, J. (2002). SST anomalies of ENSO and the Madden-Julian oscillation in the equatorial Pacific. *Journal of Climate*, *15*(17), 2429–2445. https://doi.org/10.1175/1520-0442(2002)015<2429:SAOEAT>2.0.CO;2

Zhang, C. D. (2001). Intraseasonal perturbations in sea surface temperatures of the equatorial eastern Pacific and their association with the Madden-Julian Oscillation. *Journal of Climate*, *14*(6), 1309–1322. https://doi.org/10.1175/1520-0442(2001)014<1309:IPISST>2.0.CO;2

Zhang, H.-M., Bates, J. J., & Reynolds, R. W. (2006). Assessment of composite global sampling: Sea surface wind speed. *Geophysical Research Letters*, *33*, L17714. https://doi.org/10.1029/2006GL027086

Zhao, X., Yuan, D., Yang, G., Wang, J., Liu, H., Zhang, R., & Han, W. (2019). Interannual variability and dynamics of intraseasonal wind rectification in the equatorial Pacific Ocean. *Climate Dynamics*, *52*(7-8), 4351–4369. https://doi.org/10.1007/s00382-018-4383-0

Zhu, J., Kumar, A., Huang, B., Balmaseda, M. A., Hu, Z.-Z., Marx, L., & Kinter, J. L. (2016). The role of off-equatorial surface temperature anomalies in the 2014 El Niño prediction. *Scientific Reports*, *6*(1), 19677. https://doi.org/10.1038/srep19677